MATERIALS SCIENCE

Hierarchical and reconfigurable interfibrous interface of bioinspired Bouligand structure enabled by moderate orderliness

Si-Ming Chen[1]†, Guang-Zhen Wang[1]†, YuanZhen Hou[2]†, Xiao-Nian Yang[3], Si-Chao Zhang[1], ZiBo Zhu[2], JiaHao Li[2], Huai-Ling Gao[1,2]*, Yin-Bo Zhu[2]*, HengAn Wu[2], Shu-Hong Yu[1,4]*

Introducing natural Bouligand structure into synthetics is expected to develop high-performance structural materials. Interfibrous interface is critical to load transfer, and mechanical functionality of bioinspired Bouligand structure yet receives little attention. Here, we propose one kind of hierarchical and reconfigurable interfibrous interface based on moderate orderliness to mechanically reinforce bioinspired Bouligand structure. The interface imparted by moderate alignment of adaptable networked nanofibers hierarchically includes nanofiber interlocking and hydrogen-bonding (HB) network bridging, being expected to facilitate load transfer and structural stability through dynamic adjustment in terms of nanofiber sliding and HB breaking-reforming. As one demonstration, the hierarchical and reconfigurable interfibrous interface is constructed based on moderate alignment of networked bacterial cellulose nanofibers. We show that the resultant bioinspired Bouligand structural material exhibits unusual strengthening and toughening mechanisms dominated by interface-microstructure multiscale coupling. The proposed interfibrous interface enabled by moderate orderliness would provide mechanical insight into the assembly of widely existing networked nanofiber building blocks toward high-performance macroscopic bioinspired structural assemblies.

INTRODUCTION

Fiber-based hierarchical structure is widespread in mechanically superior biological tissues (*1*, *2*). Bouligand structure composed of twist-stacked nanofiber lamellae is one typical case (*2*). Many tissues such as the hammer of stomatopod, fish scale, and lobster underbelly exhibit Bouligand structural characteristics and thus amazing mechanical properties (*3*–*6*). Structural bionics has been proven as a promising path to creating advanced materials (*1*, *2*, *7*–*11*). Under such circumstances, flexible replication of natural Bouligand structure attracts increasing attention aiming to develop high-performance structural materials (*12*–*14*).

Various fiber building blocks (such as long/short fibers, biomass/synthetic fibers, and organic/inorganic fibers) and fiber assembly strategies (such as self-assembly and artificial assembly) have been developed for the construction of bioinspired Bouligand structural materials. More specifically, long fiber–based impact-resistant materials [such as nylon-epoxy composite and polyvinyl alcohol (PVA) hydrogel] and lightweight and strong silk materials with bioinspired Bouligand structure were fabricated via electrospinning and textile processing (*15*–*17*). Discrete organic cellulose/chitin nanocrystals and inorganic $NiMoO_4{\cdot}xH_2O$ nanowires can be helically aligned for bioinspired Bouligand structure by self-assembly and the Langmuir-Schaefer assembly (*18*–*20*). In addition, external field–assisted assembly strategies such as electric field–assisted additive manufacturing and sliding shear force field–assisted programmable brushing were also developed to align discontinuous micro/nanofibers (such as carbon nanotube, hydroxyapatite microfiber, and xonotlite nanofiber) into macroscopic bioinspired Bouligand structural assemblies (*13*, *21*, *22*).

Although considerable progress has been made, most studies focused on the establishment of fiber assembly strategies and the assembly of different raw materials, efforts in interfacial design of micro/nanofiber building blocks for boosting interfibrous load transfer, and mechanical functionality of bioinspired Bouligand structure are still deficient. Impressively, natural Bouligand tissues are brilliant at the interfibrous interface, with mineralized nanoparticles or polymeric networked matrix tightly connecting adjacent nanofibers, and with pore canal fibers or fibrillar strands pinning nanofiber lamellae along the thickness direction (TD) (*5*, *23*–*25*). Ingenious biointerfaces can stabilize the Bouligand structure and simultaneously allow nanofiber micromovement for toughening. Unfortunately, how to design interfibrous interface of bioinspired Bouligand structure to realize high structural stability while maintaining movement activity of fiber building blocks for macroscopic mechanical reinforcement remains largely unexplored.

Here, we propose a design concept of hierarchical and reconfigurable interfibrous interface for bioinspired Bouligand structure based on moderate alignment of networked nanofiber building blocks (Fig. 1, A to D). The hierarchical interfibrous interface refers to nanofiber interlocking and three-dimensional (3D) hydrogen-bonding (HB) network bridging that fundamentally arises from networked nanofiber reorganizing-aligning-densifying process (Fig. 1, B and E). Different from the conventional chemical cross-linking (curing) for bioinspired interfacial design, the hierarchical interfibrous interface is adaptively dynamic to extensively disperse multidirectional

[1]Department of Chemistry, New Cornerstone Science Laboratory, Institute of Biomimetic Materials & Chemistry, Anhui Engineering Laboratory of Biomimetic Materials, Division of Nanomaterials & Chemistry, Hefei National Research Center for Physical Sciences at the Microscale, University of Science and Technology of China, Hefei 230026, China. [2]CAS Key Laboratory of Mechanical Behavior and Design of Materials, Department of Modern Mechanics, University of Science and Technology of China, Hefei 230027, China. [3]Department of Dental Implant Center, Stomatologic Hospital and College, Key Laboratory of Oral Diseases Research of Anhui Province, Anhui Medical University, Hefei 230032, China. [4]Institute of Innovative Materials, Department of Materials Science and Engineering, Department of Chemistry, Southern University of Science and Technology, Shenzhen 518055, China.
*Corresponding author. Email: ghuailing@ustc.edu.cn (H.-L.G.); zhuyinbo@ustc.edu.cn (Y.B.Z.); shyu@ustc.edu.cn (S.-H.Y.)
†These authors contributed equally to this work.

(in-plane and out-of-plane) loads via the relative sliding of nanofibers and the breaking-reforming of HBs (Fig. 1F). Using networked bacterial cellulose (BC) nanofibers (fig. S1) with rich hydroxyl (-OH) functional groups (*26*), as one demonstration, we construct hierarchical and reconfigurable interfibrous interface and fabricate bioinspired Bouligand structural material with moderate orderliness via sequentially stretching, twist-stacking, and densifying BC films (SBC) (Fig. 1, A to D, and fig. S2). Multimodal structural, mechanical, and biological studies show that the resultant SBC-based bioinspired Bouligand structural material (SBCB) exhibits excellent mechanical performance fortified by hierarchical and reconfigurable interfibrous interface, showing large potentials for repairing energy-dissipating fibrous cartilages. The proposed hierarchical and reconfigurable interfibrous interface of bioinspired Bouligand structure enabled by

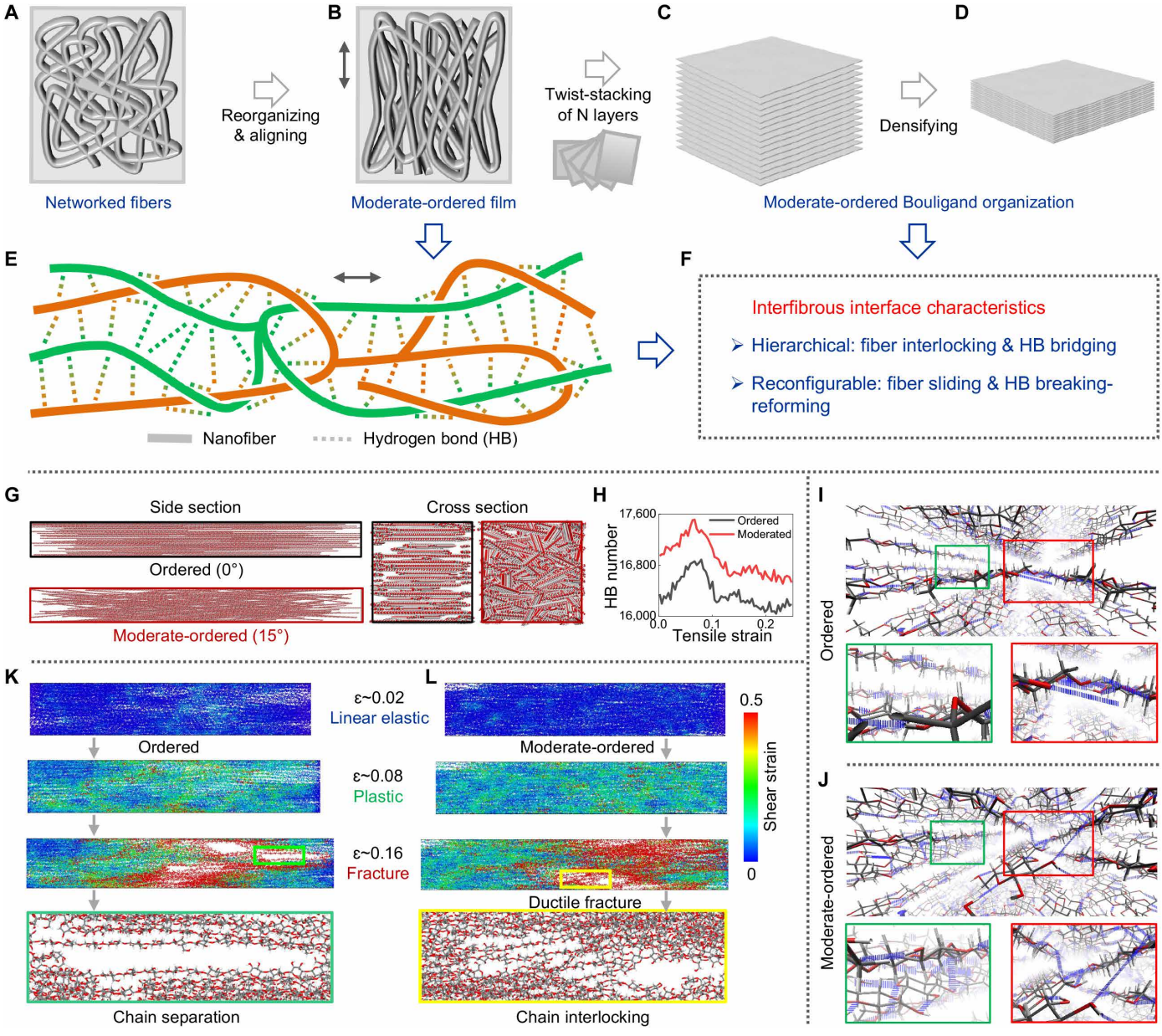

Fig. 1. Hierarchical and reconfigurable interfibrous interface of bioinspired Bouligand structure enabled by moderate orderliness. (**A** to **D**) Schematic of fabricating moderate-ordered bioinspired Bouligand structure based on networked nanofibers. (**E** and **F**) Hierarchical and reconfigurable interfibrous interface of the moderate-ordered bioinspired Bouligand structure. (**G**) Side-sectional and cross-sectional snapshots of the initial simulated ordered (0° orientation angle) and moderate-ordered (15° orientation angle) models assembled by cellulose chains. (**H**) Number and evolution of HBs as the function of tensile strain. (**I** and **J**) 3D snapshots of the initial simulated ordered model and moderate-ordered model, showing the more stereoscopic HB (blue line) network bridging within the latter. (**K** and **L**) Snapshots of the ordered and moderate-ordered models at three typical deformation stages. The shear strain distribution indicates the relative sliding of cellulose chains at the plastic stage and the stronger failure-resistant capability of the moderate-ordered model. Enlarged snapshots show chain interlocking within the moderate-ordered model and chain separation within the ordered model.

moderate orderliness would provide useful insights into the mechanical reinforcement design of nanocellulose materials and be beneficial for assembling networked nanofiber building blocks into high-performance bioinspired Bouligand structural materials for applications.

RESULTS

Moderate orderliness and hierarchical and reconfigurable interfibrous interface

Uniaxial stretching is used to align adaptable networked BC nanofibers. In the meantime, it can be used to shorten the interfibrous distance to facilitate nanofiber interlocking and HB 3D networking (Fig. 1, B, E, and F), both of which make up the hierarchical interfibrous interface (interaction) that we envision. Instead of directly clamping samples for stretching, a self-holding roll technique is used to mitigate stress concentration and premature failure at the clamping positions (fig. S2A). After being stretched, hydrated BC slices will undergo a confined-drying process (fig. S2B) (*27*). We can achieve a maximum of 30% stretching ratio (SR). Perhaps a higher SR can be expected by pretreating slices (*28*), but anyway, BC nanofibers cannot be perfectly aligned but are moderately ordered (Fig. 1B). The essential effect of BC nanofiber alignment on the interfibrous interaction (i.e., spatial HB network) cannot be nonnegligible, which largely influences the macroscopic mechanical properties from bottom to up (*29*, *30*). However, it is difficult to experimentally study the effect of the precise orientation of networked BC nanofibers and HBs on mechanical properties. Toward this end, large-scale molecular dynamics (MD) simulation, as one powerful tool, is used for quantitative investigation and theoretical analysis.

We first establish some assembly models of numerous cellulose molecular chains with different spatial orientation angles (0°, 10°, 15°, 20°, and 25°) that deviate from stretching direction (SD) (Fig. 1G and fig. S3). These static models show structural consistency with real situations to some extent: For the 0° model with high structural orderliness (representing the stretching limit), long cellulose molecular chains are not strictly parallel-aligned in in-plane direction; for small angle–oriented models, long cellulose molecular chains exhibit obvious nonparallel and entangled arrangements. Uniaxial tension simulation is then conducted to study the effect of structural orientation on mechanical properties. The ultimate strength (and toughness) of small-angle (10° and 15°) deviate-oriented models are superior to the 0° model (fig. S4A). From the perspective of stress-strain curves, the tension-to-fracture process can be divided into linear elastic stage, nonlinear plastic stage, and failure stage (fig. S4A). Young's modulus of different models maintains consistently within the linear elastic stage (strain below ~0.025), attributed to the uniform deformation of overall cellulose chains. When it comes to the plastic stage, the small angle–oriented models show an obvious strain-hardening effect and obtain optimal ultimate strength near the 15° orientation angle (fig. S4A). Considering the weakened strength of models at the orientation angle over 15°, it can be inferred that the appropriate spatial HB network plays an important role during the tension-induced interchain relative sliding process, in addition to the structural orientation.

Further, the HB analysis manifests that the number of HBs in small angle–oriented models is higher than the 0° (ordered) model and reaches an optimal value at 15°, which is consistent with the variation trend of tensile strength (Fig. 1H and fig. S4, B and C). The inference about the number of HBs is further corroborated by the Fourier transform infrared spectroscopy (FTIR) spectra of simulated molecular models with different spatial orientation angles (fig. S5) because the lowering wave number of -OH always indicates high quality and a large number of HBs (*31*–*33*). Compared to the 0° (ordered) model with a quasi-2D HB network (Fig. 1I), the interpenetrating-chain system [such as a 15° (moderate-ordered) model] provides the structural basis for building a stereoscopic 3D HB network (Fig. 1J), thus optimizing the spatial distribution and density of HBs. On the one hand, the spatial bridging effect by 3D HB network enhances the load transfer capacity and failure-resistant stability; on the other hand, more energy dissipation based on HB breaking-reforming events is introduced in the plastic deformation stage (*34*, *35*). Figure 1H and figs. S4 and S6 further demonstrate that the number of HBs increases with the tensile strain, contributing to the strain hardening in the plastic deformation stage. Moreover, the simulated snapshots at the critical failure state indicate that the interpenetrating-chain system [15° (moderate-ordered) model] promotes fiber-like chain interlocking and bridging, thus facilitating ductile fracture rather than brittle fracture [0° (ordered) model with chain separation] (Fig. 1, K and L, and movies S1 and S2). The structure with an orientation angle over 15° will diminish the alignment of cellulose chains and descend the spatial density of HBs, thus exhibiting decreased mechanical properties (fig. S4) (*36*). The reduced spatial density of HBs based on simulation can be partly proved by experimental FTIR spectra of original BC film (OBC), SBC with 15% SR, and SBC with 30% SR (fig. S7) (*31*–*33*).

Overall, the generation of interpenetrating microstructure can optimize spatial HB network dimension and promote chain interlocking but weaken structural alignment. Such contradictory effects will produce a moderate orderliness of chain assemblies to acquire optimal interchain interface and thus optimal mechanical properties. The moderate orderliness design can work synergistically at both levels of interface and microstructure. It is not that the smaller the orientation angle, the higher the mechanical properties, reflecting the trade-off of structural orientation, chain interlocking, and HB network. Although the simulations are based on cellulose molecular chains instead of nanofibers, the intrinsic mechanisms of structural orientation, chain interlocking, HB network, and their evolutions are consistent (*34*–*37*). The moderate orderliness and its derived hierarchical and reconfigurable interfibrous interface (chain interlocking and HB network bridging) would provide insights into the mechanical reinforcement design of macroscopic nanofiber assemblies.

Interfibrous interface and nanofiber micromovement of SBC with moderate orderliness

Weighing the simulations (highlighting moderate design) and natural Bouligand tissues (highlighting precise design), as one demonstration, we simplistically choose the SBCs with 30% SR as unidirectional lamellae to construct hierarchical interfibrous interface and then fabricate moderate-ordered bioinspired Bouligand structural material (Fig. 1, A to F). The unidirectional films mentioned in the following are all films with 30% SR. Distinct from OBC that is naturally intertwined, SBC exhibits nanofiber alignment partly by scanning electron microscope (SEM) observation (Fig. 2, A to C). Under cross-polarizing light, two cross-stacked SBCs exhibit an obvious light shading effect (fig. S8A), implying nanofiber alignment and global structural uniformness

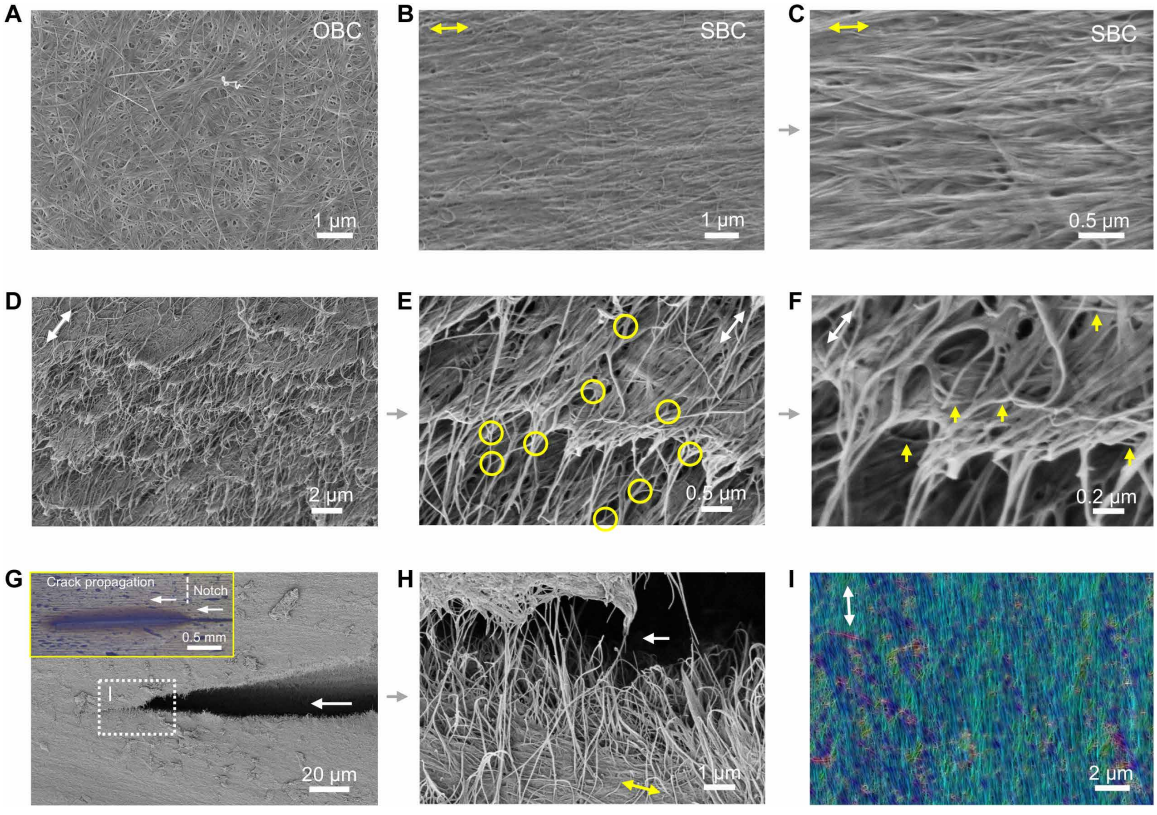

Fig. 2. Nanofiber interlocking and micromovement within moderate-ordered SBC. (**A**) SEM image of OBC showing naturally disordered nanofibers. (**B** and **C**) SEM image of SBC showing moderate nanofiber orientation. Arrows indicate SD. (**D** to **F**) SEM images of SBC's inclined cross section. White arrows indicate SD, circles indicate nanofiber branching, and yellow arrows indicate interlaced nanofibers. (**G** and **H**) SEM images of prenotched SBC's surface under tensile loading. Inset (G) is an OM image showing crack propagation. White arrows [(G) and (H)] indicate crack direction, and yellow arrow (H) indicates MADN. (**I**) False-color SEM image of SBC surface. The arrow indicates SD. Warm-colored zones partly indicate nonparallel and entangled nanofibers (non-MADN).

of SBC (*38*). Small-angle x-ray scattering (SAXS) patterns and integral curves of both unidirectional- and cross-stacked SBC laminates exhibit azimuthal intensity features (fig. S8, B to D) (*39*), further implying the structural orderliness. Note that the azimuthal intensity is not very sharp, partly verifying the nonparallel and entangled alignment of nanofibers within SBC.

Using graph theory (GT)–based structural analysis, we can quantify the nanofiber interlocking (or entangled alignment) within SBC by extracting the clustering coefficient from surface SEM image (*40*, *41*). Studies show that the clustering coefficient of SBC is 0.10642 and higher than that of OBC (0.06764) possibly due to the stretching-induced densification process (figs. S9 and S10). A relatively high value of clustering coefficient indicates that nanofiber interlocking exists robustly in SBC. We further investigate the internal structure of SBC via fracture cross-sectional analysis. It is expected that extensive pull-out of main-aligned-directional nanofibers (MADNs) can be found (Fig. 2D). The alignment direction of MADN is parallel to SD indicated by arrow (Fig. 2D). Further, nanofiber branching (circles) and interlacement (yellow arrows) are found (Fig. 2, E and F). Quantitatively, the clustering coefficient from the fracture cross-sectional SEM image of SBC is 0.08873 (fig. S11). Under such circumstances, the hierarchical interfibrous interface including nanofiber interlocking as well as 3D HB network bridging within SBC can be expected.

The hierarchical interfibrous interface can affect the mechanical properties of macroscopic nanofiber assemblies (*35*, *42*). Here, we apply tensile load to crack the prenotched SBC (notch direction is parallel to SD; loading direction (LD) is perpendicular to SD) to investigate the interface behavior and movement activity of nanofibers. A large shadow zone around crack can be found after tensile loading (Fig. 2G, inset), implying extensive load transfer and energy dissipation. Further, curving, rotation, and bridging of nanofibers can be found at the shadow zone (Fig. 2, G and H, and fig. S12). The extensive nanofiber micromovement (internal cause of shadow zone formation) is initially driven by non-MADN (warm-colored zones in Fig. 2I) because the pre-crack direction is inconsistent with the long-axis direction of non-MADN; further, it is collaboratively contributed by non-MADN and MADN due to their interconnected networked characteristic. It can be speculated that the hierarchical interfibrous interface (nanofiber interlocking and HB network bridging) is organized and dynamic, enabling non-MADN and MADN to collaboratively move to adapt to external loads. The hierarchical and reconfigurable interfibrous interface, fundamentally endowed by the moderate alignment of adaptable networked nanofibers, different from the previously reported nonreversible chemical cross-linking (curing) for bioinspired interfacial design (*1*, *9*, *43*), can facilitate extensive load transfer and avoid sudden catastrophic failure.

Mechanical superiorities of SBCB endowed by moderate orderliness and interfibrous interface

We can introduce the hierarchical and reconfigurable interfibrous interface into bioinspired SBCB via bottom-up assembly (twist-stacking and densifying SBCs) (Fig. 1, C and D). The smaller the interlamellar twisted angle, the better the performance of the bioinspired Bouligand structure (*6*, *22*). Twenty-degree twisted angle is set by referring to our previous work (*22*) and natural Bouligand tissues (*4*, *6*, *16*). Experimentally, polyhydric PVA with strong HB formation capability exhibits good wettability and can fill the micro/nanoscale ravines of SBC (fig. S13, A and B); it, therefore, is used as an interlamellar adhesive. As shown in the cross section of bioinspired SBCB (fig. S13, C to F), twisted alignment of nanofibers can be found. Moreover, under cross-polarizing light, much larger-scale twisted alignment can be detected via the brightness-and-color evolution of nanofiber assemblies (*13*, *38*, *44*). Specifically, when a cross section containing predesigned two twist-aligned lamellae (fig. S13, G to I) is rotated 20°, it can uniformly change in brightness and color along TD (fig. S13, J to L) (*45*). This kind of structure-optics relatedness confirms the global twisted alignment of nanofibers, which is the precondition of bioinspired Bouligand structural design. In addition, it also inspires a convenient optical way to investigate interfibrous interface–mediated nanofiber micromovement and structural evolution of bioinspired assemblies.

Beyond natural Bouligand tissues and most reported bioinspired Bouligand structural materials (highlighting precise assembly of discrete fibers) that are considered to be isotropic, the moderate-ordered bioinspired SBCB with hierarchical and reconfigurable interfibrous interface exhibits hierarchical isotropy. The isotropy relates to not only the twisted alignment of SBCs but also the moderate alignment of networked BC nanofibers within SBC. Single lamella is the basis of bioinspired Bouligand structure. SBC can flexibly adapt to in-plane tensile load via hierarchical and reconfigurable interfibrous interface–mediated nanofiber micromovement and HB breaking-reforming. Specifically, when LD is parallel to SD, most nanofibers can further straighten (Fig. 3A, top), which is reflected by the color variation and homogenization of SBC under in situ tensile loading and cross-polarizing light (Fig. 3B, top, and movie S3). When LD deviates (20°) from SD, non-MADN can move first and drive MADN reorientation (Fig. 3A, bottom) without causing severe in-plane interfibrous dissociation. This inference is analogously reflected by the color variation and structural integrity of SBC (Fig. 3B, bottom, and movie S4).

In addition, the nanofiber reorientation can be directly detected by SEM. As shown in the cross section containing three twist-aligned lamellae (white arrows) (Fig. 3C), most nanofibers can reorient to LD (yellow arrow), reflecting the adaptability of networked nanofibers to external load. Moreover, the nanofiber micromovement can be monitored by SAXS. As shown in Fig. 3 (D to F), the SAXS patterns of bioinspired SBCB under tensile loading can occur in directional protrusions based on the original roundness (indicating SBCB's isotropy). The appearance and shift of peaks in the integral curves (Fig. 3G) further provide evidence of nanofiber micromovement and reorientation. It can be speculated that, compared to the conventional bioinspired Bouligand structural materials, the moderate-ordered bioinspired SBCB can extensively transfer loads via hierarchical and reconfigurable interfibrous interface–mediated nanofiber micromovement and HB breaking-reforming. As expected, bioinspired SBCB exhibits mechanical insensitivity to tensile LD (Fig. 3, H to J). When LD is parallel to the SD of one SBC, the peak force and energy absorption are 33.82 and 68.03 N mm; when LD is parallel to the bisector direction of two neighboring SBCs, the peak force and energy absorption are 32.23 and 63.10 N mm.

In addition to contributing to resisting in-plane tensile load, the hierarchical and reconfigurable interfibrous interface also imparts bioinspired SBCB with excellent capability to resist out-of-plane loads. When responding to puncture load, the constructed bioinspired Bouligand structure with moderate orderliness is more dominant than the conventional bioinspired Bouligand structure. Specifically, single moderate-ordered lamella can effectively transfer and disperse load from the initial load-bearing point via nanofiber micromovement and HB breaking-reforming mediated by hierarchical and reconfigurable interfibrous interface. Thus, the stress-affected area is large but the actual failure area is small (Fig. 4A). In contrast, without a strong interfibrous interface for transferring loads, the strictly unidirectional lamella within the conventional bioinspired Bouligand structure will cause stress concentration and then severe anisotropic damage (such as interfibrous dissociation) for releasing stress (Fig. 4B). One 3D-printed bioinspired Bouligand model with strict fiber alignment showing severe interfibrous slit (fig. S14) qualitatively corroborates our viewpoint.

Overall, compared to the conventional bioinspired Bouligand structure, the moderate-ordered bioinspired Bouligand structure with hierarchical and reconfigurable interfibrous interface owns rich load transfer pathways and thus improved structural stability. Note that the OBC laminate exhibits natural isotropy, partly implying effective dispersion of out-of-plane loads, but it exhibits poor performance due to low density and a lack of an organized direction-reinforcement structure. Mechanical investigation shows that the peak force and energy to puncture of bioinspired SBCB (16.13 and 3.64 N mm) are much higher than those of SBCs (13.79 and 2.98 N mm) and OBCs (10.31 and 2.03 N mm) (Fig. 4, C to E). Optical observation of punctured zones reveals that bioinspired SBCB exhibits a small damaged area (circle) without crack propagation (Fig. 4F), while SBCs exhibits large damage with cracks (arrows) (Fig. 4G). Note that the cracks are tortuous and different from those generated in strictly unidirectional materials (fig. S14), implying crack deflection for toughening caused by the moderately aligned and interlocked nanofibers. In contrast, OBCs exhibits unpredictable crack proliferation for releasing stress (Fig. 4H).

Bioinspired SBCB with hierarchical and reconfigurable interfibrous interface, extensive load transfer capability, and benign components exhibits large potentials for biomedical applications such as repairing energy-dissipating fibrous cartilages. Exogenous repairing materials are often perforated for fixation. Because of the in vivo load complexity, stress concentration inevitably occurs at the fixation positions and then causes severe crack proliferation. Considering this scenario, we investigate the crack resistance of bioinspired SBCB via directionally loading one preinserted nail (fig. S15A). Load-displacement curves imply that the peak force of bioinspired SBCB is relatively high compared to SBCs and OBCs (fig. S15B). For bioinspired SBCB, the pre-crack is hard to propagate from any direction because it is surrounded by the helical-aligned lamellae. In other words, the hierarchically isotropic bioinspired SBCB sets strong crack stoppers in all directions, which is different from SBCs with one unidirectional crack stopper and OBCs without organized crack stoppers. Not limited to cracking at the fixation positions, exogenous repairing materials unpredictably give rise to tearing accidents. The crack resistance is further investigated by prenotched tear tests (fig. S16). Because of low unidirectional-reinforcement ratio compared to SBCs, bioinspired SBCB exhibits moderate load resistance. Note that its structural stability is superior to that of SBCs due

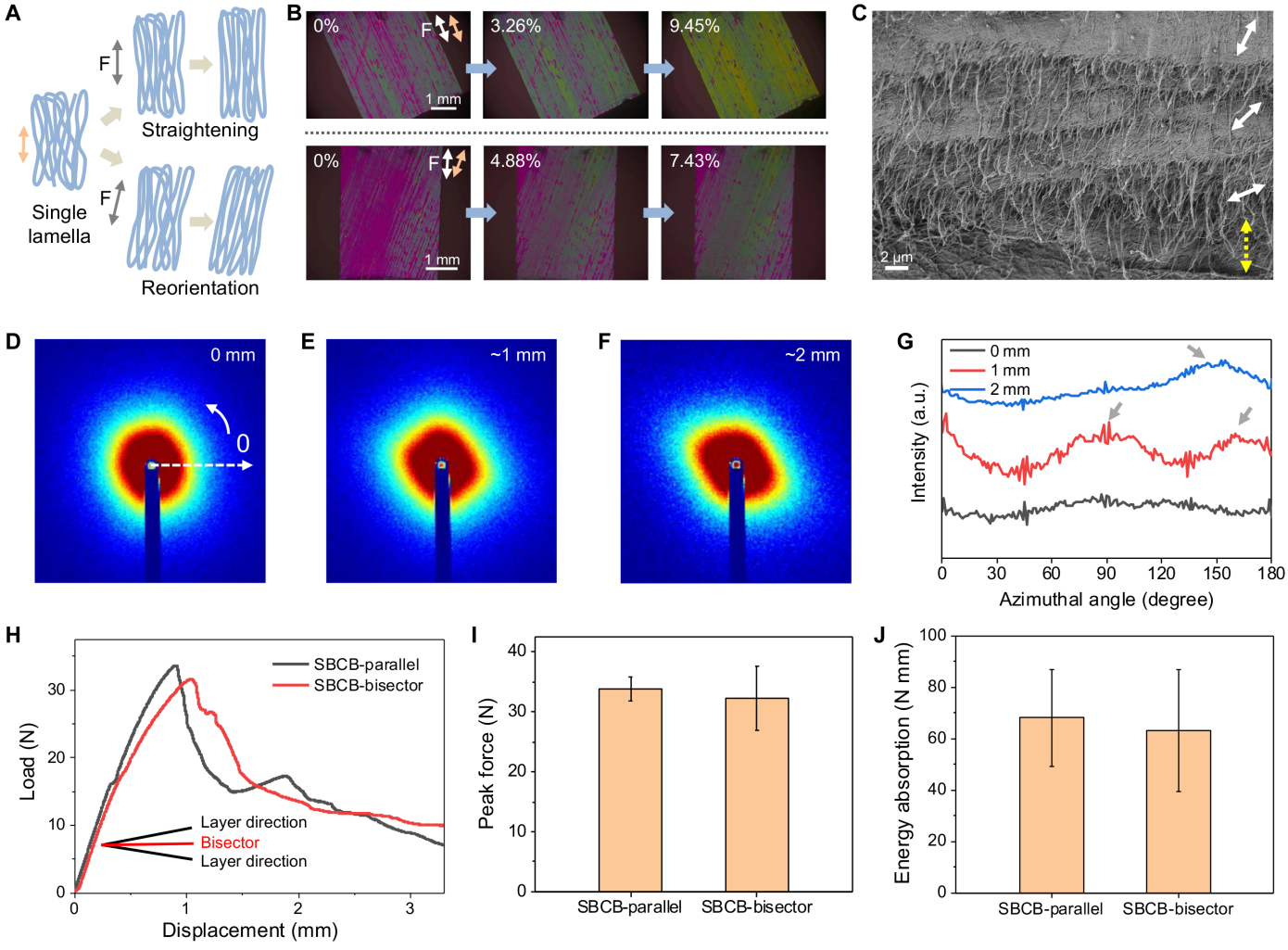

Fig. 3. Hierarchical and reconfigurable interfibrous interface–enabled extensive nanofiber micromovement under in-plane tensile loading and hierarchical isotropy of bioinspired SBCB. (**A**) Schematic of structural evolution of SBC under different LDs. When LD is parallel to SD (amber arrow), nanofibers can be straightened; when it deviates from SD, nanofibers can be reoriented. (**B**) Polarized optical microscopy (POM) images of SBC under in situ tensile loading (with different LDs). White arrows indicate LD, and amber arrows indicate SD. (**C**) SEM image of bioinspired SBCB's cross section showing nanofiber reorientation. White arrows indicate the SD of three lamellae, and yellow arrow indicates the reorientation direction. Most nanofibers within three lamellae are reoriented. (**D** to **F**) SAXS patterns of bioinspired SBCB under tensile loading. As displacement increases, patterns change directionally, implying nanofiber reorientation. (**G**) Integral curves based on SAXS patterns. The appearance and shift of peaks (arrows) imply nanofiber reorientation. (**H** to **J**) Mechanical insensitivity of bioinspired SBCB to LD. LD is parallel to SD of the top lamella and neighboring lamellae bisector direction, respectively. The sample size is 3 mm (width) by 15 mm (length), the gauge length is 5 mm, and the loading rate is 0.005 mm s^{-1}. All the error bars represent the standard deviation of at least three replicate measurements.

to hierarchical isotropy and well-interlamellar coupling capability. It thus can dissipate a lot of energy responding to tear load (fig. S16C).

Wet mechanical properties and application prospect of SBCB

Wet conditions in vivo lead us to investigate the tear resistance of hydrated bioinspired SBCB. Water, widely existing in natural Bouligand tissues (such as fish scale and lobster underbelly) (*3*, *4*, *46*), can facilitate the cellulose-water molecule-cellulose HB formation and reduce the interfacial energy barrier required to overcome, thus boosting nanofiber sliding and producing more energy dissipation behaviors of bioinspired SBCB (*22*, *35*). In other words, the introduction of water molecules can further stimulate the already high movement activity of nanofibers within bioinspired SBCB. Mechanical studies show that the energy absorption of hydrated bioinspired SBCB is 28.28 N mm, which is 6.31 times that of dry bioinspired SBCB (4.48 N mm) (fig. S16C) and is still at a high level compared to that of hydrated SBCs (17.33/9.48 N mm) (Fig. 5, A to C).

As mentioned earlier, nanofiber orientation can correlate with color under cross-polarizing light (fig. S13, J to L), which provides convenience for detecting nanofiber micromovement and load transfer. As shown in Fig. 5D, the positions (top right and bottom right) away from the crack exhibit relatively uniform color, implying the global structural uniformness of bioinspired SBCB. The position around the crack tip evolves to be multicolored, implying nanofiber micromovement and structural change. Note that the nanofiber micromovement is not confined to one single lamella but multiple lamellae because the color appearance is not uniform, which is different from the earlier observation of two twist-aligned lamellae (fig. S13, J

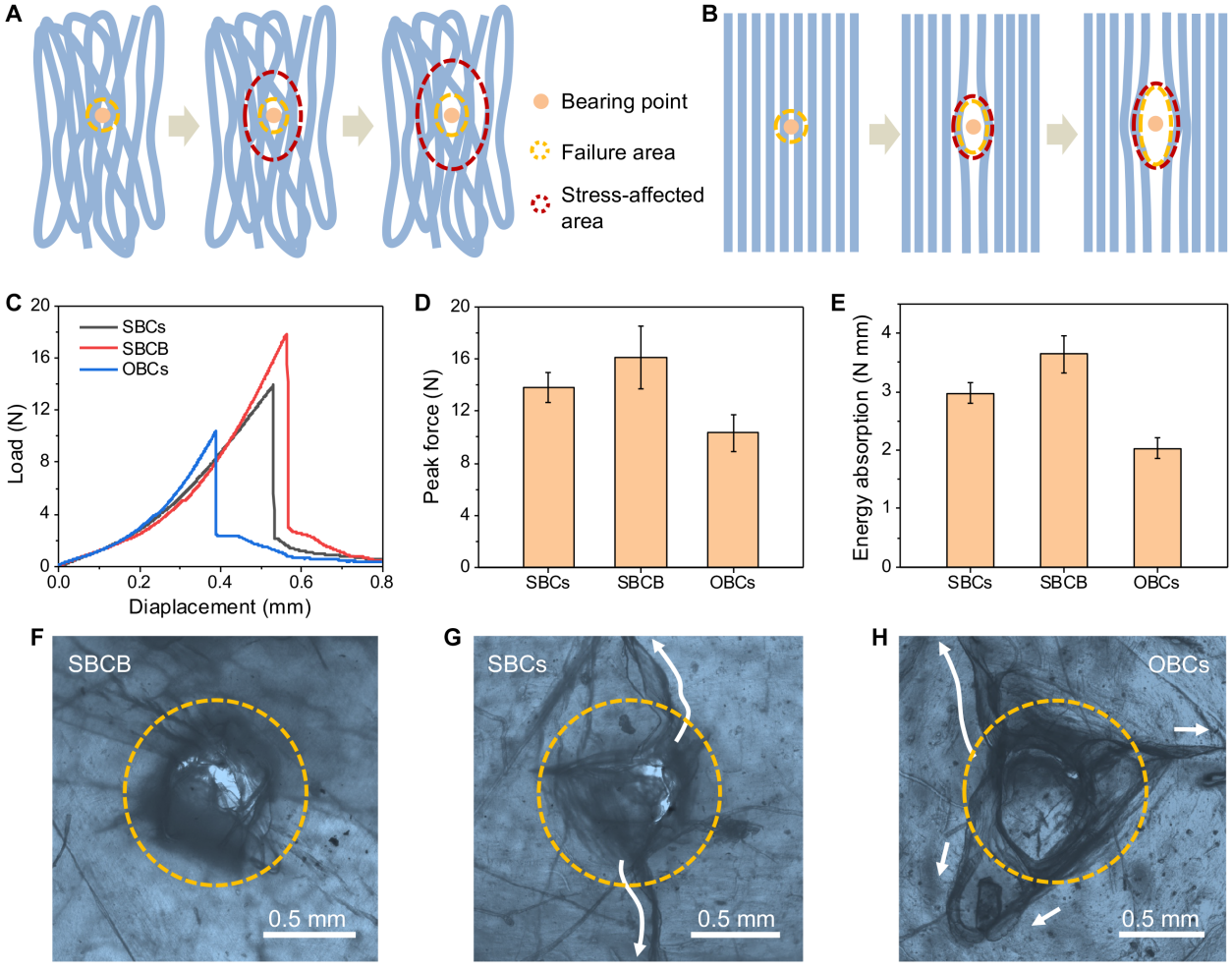

Fig. 4. Hierarchical and reconfigurable interfibrous interface–enabled extensive load transfer of bioinspired SBCB under (out-of-plane) puncture loading. (**A** and **B**) Puncture scenarios of one single SBC within bioinspired SBCB and one strictly unidirectional lamella within the conventional bioinspired Bouligand structure. Yellow points and circles and red circles indicate force-bearing points, failure areas, and stress-affected areas, respectively. (**C** to **E**) Load-displacement curves, peak force, and energy absorption of bioinspired SBCB, SBCs, and OBCs. (**F** to **H**) OM images of punctured (0.5-mm-diameter needle) zones of bioinspired SBCB, SBCs, and OBCs. Circles indicate the main damaged areas. Arrows indicate crack propagation. All the error bars represent the standard deviation of at least three replicate measurements.

to L). The large-area multicolored zone (Fig. 5E) reflects extensive nanofiber micromovement, load transfer, and energy dissipation endowed by the hierarchical and reconfigurable interfibrous interface that is mediated by water molecules. Zooming in on the crack tip further reveals rough fracture morphology (Fig. 5F), implying twisted crack propagation along TD to dissipate energy (*22*).

Compared to optical observation, SEM can provide more direct and subtle structural information here. As shown in Fig. 5G, large-area stria can be found, verifying the abovementioned extensive load transfer. The stria direction (yellow arrow in Fig. 5G) and nanofiber alignment direction (arrow in Fig. 5H) are approximately consistent. Further, nanofibers at the low-positioned lamellae are found to reorient toward the stria direction by curving and rotation (Fig. 5, G, I, and J). Specifically, in Fig. 5J, yellow arrow and white arrow indicate the original orientation direction and reorientation direction, respectively, and color-gradient curved lines show nanofiber reorientation. Overall, the direction convergence between nanofiber alignment and stria indicates flexible responses of the moderate-ordered bioinspired SBCB to external loads. It can be speculated that, for the networked nanofiber building blocks, the moderate-ordered bioinspired Bouligand structure with hierarchical and reconfigurable interfibrous interface represents one kind of mechanically optimal structure. Integrating the advantages of high mechanical performance, biocompatibility (Fig. 6, A to D), shape adaptability (Fig. 6, E to J), and size/weight stability (Fig. 6, K and L, and fig. S17), bioinspired SBCB is suitable for repairing complex loaded and shaped meniscus (Fig. 6, M to O) [as a demonstration, an eccentric "artificial meniscus" is envisioned (Fig. 6, P and Q)] and cartilage endplate.

DISCUSSION

In this work, focusing on the interfibrous interface that is critical to load transfer, structural stability, and mechanical functionality of bioinspired Bouligand nanofiber assemblies, we propose one kind of hierarchical and reconfigurable interfibrous interface (nanofiber

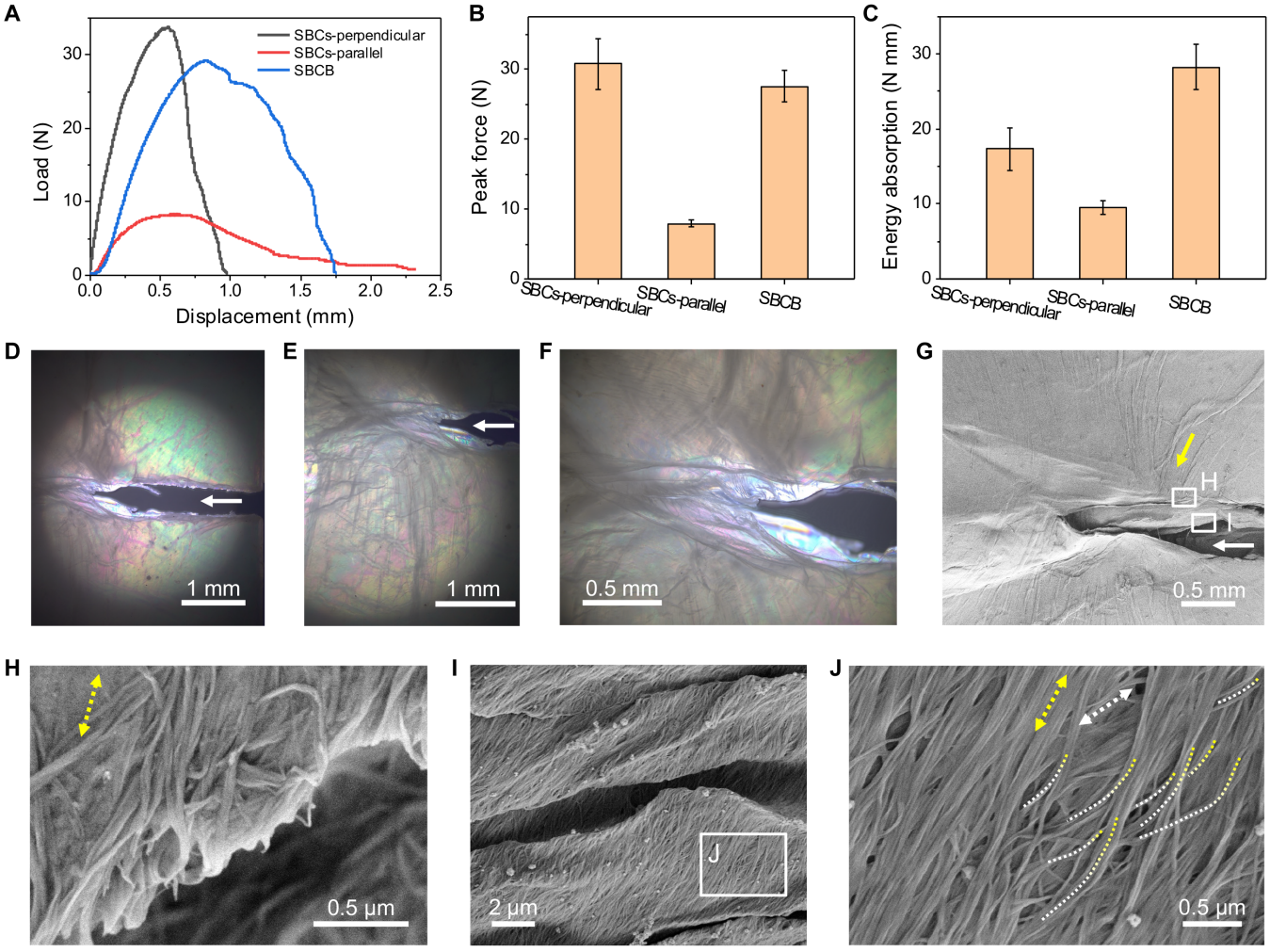

Fig. 5. Hierarchical and reconfigurable interfibrous interface–enabled extensive load transfer of bioinspired SBCB under tear loading. (**A** to **C**) Load-displacement curves, peak force, and energy absorption of wet bioinspired SBCB and SBCs. (**D** to **F**) POM images of crack tip of bioinspired SBCB. Arrow indicates crack direction. (**G**) SEM image of the crack tip and its surroundings showing obvious stria. White arrow indicates crack direction; yellow arrow indicates the stria direction near box (H). (**H**) SEM image showing nanofiber alignment (arrow). (**I**) SEM image showing relatively horizontal stria. (**J**) SEM image showing nanofiber reorientation. All the error bars represent the standard deviation of at least three replicate measurements.

interlocking and HB network bridging) based on moderate orderliness design. Through nanofiber sliding and HB breaking-reforming, the interface can adapt to multidirectional loads and facilitate energy dissipation for maintaining structural stability and mechanical functionality. Fundamentally, the moderate orderliness design here can work synergistically at both levels of interface and microstructure, finally endowing the designed materials with improved mechanical properties than previously reported bioinspired Bouligand structural materials. Overall, the proposed hierarchical and reconfigurable interfibrous interface and the moderate orderliness design of the bioinspired Bouligand structure would provide important insights into the mechanical reinforcement design of polyhydric nanocellulose materials. They can also guide the transformation of widely existing networked nanofiber building blocks into high-performance macroscopic bioinspired Bouligand structural assemblies for applications. Further, in addition to the efforts in the establishment of assembly strategies and the assembly of different raw materials, the efforts in the hierarchical interfacial design of micro/nanoscale building blocks would drive the field of bioinspired structural materials including fiber-based materials and nacre-inspired materials toward distinctive development paths.

MATERIALS AND METHODS

Materials

BC hydrated slices (2 mm thickness) were purchased (Guilin Qihong) and cut into a rectangle shape of 10 cm (width) by 30 cm (length). These slices were put into warm water (40°C) for 24 hours to swell and loosen. PVA aqueous solution (1 wt %) was prepared by powder dissolution at 90°C for 6 hours.

Stress-induced nanofiber alignment and assembly generation

To minimize stress concentration at the clamping positions, two ends of one slice were fixed via twining (fig. S2A). In this case, the uniaxial load can fully transfer to the slice. One universal mechanical

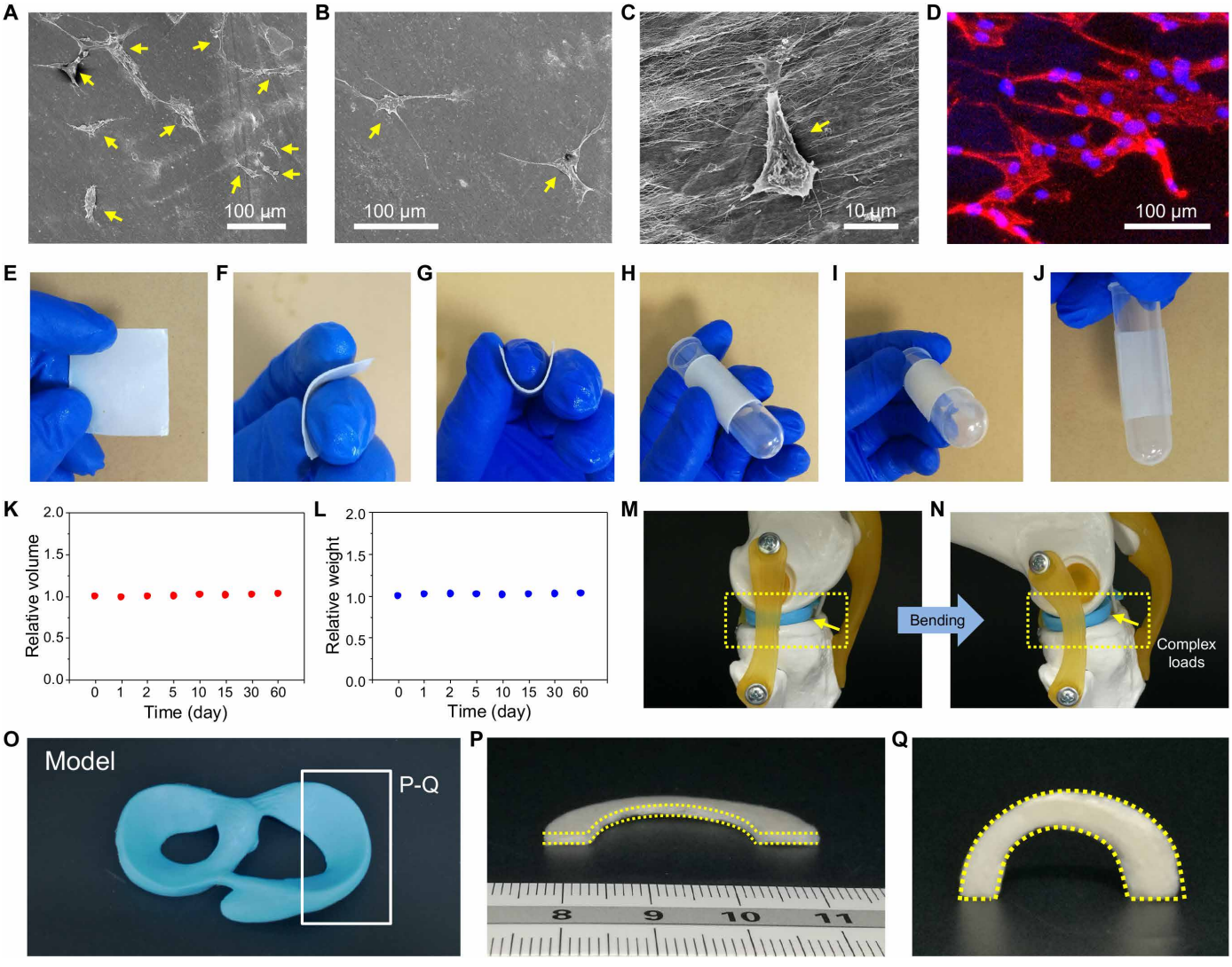

Fig. 6. Biomedical application prospects of bioinspired SBCB. (**A** to **C**) SEM images of cell-bioinspired SBCB complexes. (**D**) Confocal laser microscope image of cell-bioinspired SBCB complexes. (**E** to **J**) Hydrated bioinspired SBCB showing flexibility and adaptability. (**K** and **L**) Stability of hydrated bioinspired SBCB soaked in the phosphate-buffered saline (PBS) solution at room temperature. (**M** and **N**) Digital images of knee joint model during bending. Blue meniscus suffers complex loads. (**O**) Digital image of complex-shaped meniscus model. (**P** and **Q**) Digital images of one eccentric half-ring–shaped material.

equipment (Instron 5565-A) was used for stretching with constant displacement mode (1 mm min^{-1}). A high-power humidifier was used to wet slice. The slice can be stretched ~30% when cracking. The stretched slice was still held on clamping for 30 min to shape and then taken off and put into water (two ends were fixed) for 24 hours to further balance. Subsequently, the hydrated slice (two ends were fixed) was put on the polymethyl methacrylate substrate at 40°C until it was completely dried (fig. S2B). The original slice was dried directly (without stretching) to get OBC. With PVA as adhesive, the films were stacked together to form laminates.

Sample characterizations

Optical microscopy (OM) images were acquired by an optical microscope (OLYMPUS BX53M). SEM images were acquired by equipment (Hitachi, SU8220), and samples were coated with platinum before observation. Instron 5565-A (500-N load cell) mechanical equipment was used for stretching and mechanical tests. SAXS patterns were acquired by equipment (Anton Paar SAXSpoint 2.0). FIT2D software was used to further process SAXS patterns. ImageJ software with OrientationJ plug was used to mark nanofiber orientation based on SEM image. Experimental FTIR spectra were acquired by equipment (Thermo Fisher Scientific, Nicolet iN10). Confocal laser microscopy image was acquired by equipment (CLSM, Zeiss, LSM880).

GT-based structural analysis

The GT-based analyses were performed to quantitatively characterize the interlocking of cellulose nanofibers at the nanoscale, using the relevant SEM images. The clustering coefficients from GT description of the nanofiber networks were calculated via the StructuralGT software (*40*, *41*).

Mechanical tests

For tensile tests, samples were carefully cut into 5-mm-wide and 20-mm-long stripes (150 μm thick). Tests were performed at a loading rate of 0.01 mm s^{-1} with a gauge length of 5 mm. For tear tests, samples (5 mm wide by 20 mm long by 150 μm thick) were notched to half of the width using a sharp blade. Tests were performed at a loading rate of 0.1 mm min^{-1} with a gauge length of 5 mm. For puncture tests, samples (10 mm wide by 10 mm long by 150 μm thick) were clamped on the man-made holding device that leaves a circular hollow region (5-mm diameter) in the center. The diameter of the needle tip was 500 μm; puncture loading rate was 0.01 mm s^{-1}. For nail-induced crack propagation tests, a nail (500-μm diameter) was inserted into the sample (5 mm wide by 20 mm long by 150 μm thick). For all samples, the nail was inserted into the same position. The travel rate of the nail is 0.02 mm s^{-1}. All samples were stored at a relative humidity of 50% at 25°C for 48 hours before the test. Hydrated samples were soaked in water for 48 hours before the test. Each sample contained at least five specimens.

MD simulations

MD simulations were performed by the Large-scale Atomic/Molecular Massively Parallel Simulator (LAMMPS) code package (*47*) to investigate the effect of cellulose network orientation degree on mechanical behaviors at the nanoscale. The first principles–based reactive force field was used to simulate the deformation process, which has been demonstrated to provide a reliable description of noncovalent interactions between cellulose molecules (*34*, *35*, *48*). To take the intermolecular bonding interactions and the fiber-network structural features into consideration simultaneously in our finite-scale molecular models, cellulose molecular chains were adopted to represent the high–aspect ratio cellulose nanofibers (*34*, *36*). The models of numerous cellulose molecular chains with different spatial orientation angles (0°, 10°, 15°, 20°, and 25°) that deviated from SD were established. All orientation models were composed of 150 cellulose molecular chains with 30 glucose units. The size of each model is 80 nm by 10 nm by 10 nm. Periodic boundary conditions were set perpendicular to the long axis. The time step of MD simulations was 0.5 fs. To obtain the equilibrium structure, energy minimization was first performed on all simulated systems based on the conjugate-gradient algorithm with an energy-convergence criterion. Then, the system was equilibrated for 0.5 ns in an isothermal-isobaric (NPT) ensemble at a low temperature (10 K) and a zero pressure, ensuring the minimum energy and internal stress. The uniaxial tension load was conducted by moving both ends of the assembly model along the long axis in opposite directions with a constant velocity of 0.0002 Å fs^{-1}. The NPT ensemble with pressures perpendicular to the tension direction controlled to zero was applied to the tension process. A low temperature (10 K) was chosen to suppress thermal noise and reveal the characteristic deformation mechanisms. The HB networks in initial models were displayed as blue dashed lines by the VMD Hydrogen Bonds plugin (*49*). The initial models and MD simulation snapshots were visualized by OVITO software (*50*).

FTIR spectra analysis of molecular models

The FTIR spectra calculations of simulated molecular models with different tensile strain and spatial orientation angles were conducted using LAMMPS code package and an available Python code (*47*, *51*, *52*). The LAMMPS was used to compute the net dipole moment of the system. The Python script was performed to determine the dipole-dipole autocorrelation function and execute the Fourier transform to derive the IR curves. The molecular configurations with specific tensile strain were extracted and fully equilibrated at the canonical (NVT) ensemble under a low temperature (10 K).

In vitro biocompatibility

To investigate in vitro biocompatibility and cytotoxicity of the SBCB, the cellular morphology was applied to evaluate the MC-3T3 cell line. To prepare the SBCB-conditioned medium, 200 mg of the SBCB was incubated in 10 ml of minimum essential medium (MEM) supplemented with 10% (v/v) fetal bovine serum and 1% (v/v) penicillin-streptomycin solution at 37°C for 24 hours. MC-3T3 cells were plated on the SBCB (10-mm diameter) at a density of 5.0×10^4 cells and incubated to adhere at 37°C for 2 hours in a 5% CO_2 atmosphere. The pristine MEM was supplemented, and the cells were cultured for 72 hours inside an incubator. Cell viability was assessed by a confocal microscope image for MC-3T3 cells stained by rhodamine and 4′,6-diamidino-2-phenylindole (DAPI). For SEM observation, the sample was immobilized in 4% paraformaldehyde for 40 min and dehydrated with graded ethanol. After drying, the sample was sputtered with gold and observed by SEM.

Supplementary Materials

This PDF file includes:

Figs. S1 to S17

Legends for moves S1 to S4

Other Supplementary Material for this manuscript includes the following:

Movies S1 to S4

REFERENCES AND NOTES

1. J. Peng, Q. Cheng, High-performance nanocomposites inspired by nature. *Adv. Mater.* **29**, 201702959 (2017).
2. S. Ling, D. L. Kaplan, M. J. Buehler, Nanofibrils in nature and materials engineering. *Nat. Rev. Mater.* **3**, 18016 (2018).
3. E. A. Zimmermann, B. Gludovatz, E. Schaible, N. K. Dave, W. Yang, M. A. Meyers, R. O. Ritchie, Mechanical adaptability of the Bouligand-type structure in natural dermal armour. *Nat. Commun.* **4**, 2634 (2013).
4. J. Wu, Z. Qin, L. Qu, H. Zhang, F. Deng, M. Guo, Natural hydrogel in American lobster: A soft armor with high toughness and strength. *Acta Biomater.* **88**, 102–110 (2019).
5. J. C. Weaver, G. W. Milliron, A. Miserez, K. Evans-Lutterodt, S. Herrera, I. Gallana, W. J. Mershon, B. Swanson, P. Zavattieri, E. DiMasi, D. Kisailus, The stomatopod dactyl club: A formidable damage-tolerant biological hammer. *Science* **336**, 1275–1280 (2012).
6. K. Wu, Z. Song, S. Zhang, Y. Ni, S. Cai, X. Gong, L. He, S. H. Yu, Discontinuous fibrous Bouligand architecture enabling formidable fracture resistance with crack orientation insensitivity. *Proc. Natl. Acad. Sci. U.S.A.* **117**, 15465–15472 (2020).
7. H. B. Yao, J. Ge, L. B. Mao, Y. X. Yan, S. H. Yu, 25th anniversary article: Artificial carbonate nanocrystals and layered structural nanocomposites inspired by nacre: Synthesis, fabrication and applications. *Adv. Mater.* **26**, 163–188 (2014).
8. P. Podsiadlo, A. K. Kaushik, E. M. Arruda, A. M. Waas, B. S. Shim, J. Xu, H. Nandivada, B. G. Pumplin, J. Lahann, A. Ramamoorthy, N. A. Kotov, Ultrastrong and stiff layered polymer nanocomposites. *Science* **318**, 80–83 (2007).
9. S. Wan, Y. Chen, S. Fang, S. Wang, Z. Xu, L. Jiang, R. H. Baughman, Q. Cheng, High-strength scalable graphene sheets by freezing stretch-induced alignment. *Nat. Mater.* **20**, 624–631 (2021).
10. C. Zhao, P. Zhang, J. Zhou, S. Qi, Y. Yamauchi, R. Shi, R. Fang, Y. Ishida, S. Wang, A. P. Tomsia, M. Liu, L. Jiang, Layered nanocomposites by shear-flow-induced alignment of nanosheets. *Nature* **580**, 210–215 (2020).
11. A. Mao, N. Zhao, Y. Liang, H. Bai, Mechanically efficient cellular materials inspired by cuttlebone. *Adv. Mater.* **33**, 2007348 (2021).
12. R. P. Behera, H. Le Ferrand, Impact-resistant materials inspired by the mantis shrimp's dactyl club. *Matter* **4**, 2831–2849 (2021).
13. S. M. Chen, H. L. Gao, Y. B. Zhu, H. B. Yao, L. B. Mao, Q. Y. Song, J. Xia, Z. Pan, Z. He, H. Wu, S. H. Yu, Biomimetic twisted plywood structural materials. *Natl. Sci. Rev.* **5**, 703–714 (2018).

14. H. Cölfen, Emerging artificial Bouligand-type structural materials. *Natl. Sci. Rev.* **5**, 786–787 (2018).
15. R. Chen, J. Liu, C. Yang, D. A. Weitz, H. He, D. Li, D. Chen, K. Liu, H. Bai, Transparent impact-resistant composite films with bioinspired hierarchical structure. *ACS Appl. Mater. Interfaces* **11**, 23616–23622 (2019).
16. J. Ni, S. Lin, Z. Qin, D. Veysset, X. Liu, Y. Sun, A. J. Hsieh, R. Radovitzky, K. A. Nelson, X. Zhao, Strong fatigue-resistant nanofibrous hydrogels inspired by lobster underbelly. *Matter* **4**, 1919–1934 (2021).
17. Y. Liu, Y. Li, Q. Wang, J. Ren, C. Ye, F. Li, S. Ling, Y. Liu, D. Ling, Biomimetic silk architectures outperform animal horns in strength and toughness. *Adv. Sci.* **10**, 2303058 (2023).
18. B. Wang, A. Walther, Self-assembled, iridescent, crustacean-mimetic nanocomposites with tailored periodicity and layered cuticular structure. *ACS Nano* **9**, 10637–10646 (2015).
19. S. Matsumura, S. Kajiyama, T. Nishimura, T. Kato, Formation of helically structured chitin/$CaCO_3$ hybrids through an approach inspired by the biomineralization processes of crustacean cuticles. *Small* **11**, 5127–5133 (2015).
20. J. Lv, D. Ding, X. Yang, K. Hou, X. Miao, D. Wang, B. Kou, L. Huang, Z. Tang, Biomimetic chiral photonic crystals. *Angew. Chem. Int. Ed.* **58**, 7783–7787 (2019).
21. Y. Yang, Z. Chen, X. Song, Z. Zhang, J. Zhang, K. K. Shung, Q. Zhou, Y. Chen, Biomimetic anisotropic reinforcement architectures by electrically assisted nanocomposite 3D printing. *Adv. Mater.* **29**, 201605750 (2017).
22. S. M. Chen, K. Wu, H. L. Gao, X. Sun, S. C. Zhang, X. Y. Li, Z. B. Zhang, S. M. Wen, Y. Zhu, H. Wu, Y. Ni, S. H. Yu, Biomimetic discontinuous Bouligand structural design enables high-performance nanocomposites. *Matter* **5**, 1563–1577 (2022).
23. J. Rivera, S. Murata, M. S. Hosseini, A. A. Trikanad, R. James, A. Pickle, N. Yaraghi, N. Matsumoto, W. Yang, D. Y. Parkinson, H. S. Barnard, P. Zavattieri, A. Arakaki, D. Kisailus, Structural design variations in Beetle Elytra. *Adv. Funct. Mater.* **31**, 2106468 (2021).
24. S. Yin, W. Yang, J. Kwon, A. Wat, M. A. Meyers, R. O. Ritchie, Hyperelastic phase-field fracture mechanics modeling of the toughening induced by Bouligand structures in natural materials. *J. Mech. Phys. Solids* **131**, 204–220 (2019).
25. N. A. Yaraghi, N. Guarín-Zapata, L. K. Grunenfelder, E. Hintsala, S. Bhowmick, J. M. Hiller, M. Betts, E. L. Principe, J. Y. Jung, L. Sheppard, R. Wuhrer, J. M. Kittrick, P. D. Zavattieri, D. Kisailus, A sinusoidally architected helicoidal biocomposite. *Adv. Mater.* **28**, 6835–6844 (2016).
26. Q. F. Guan, Z. M. Han, T. T. Luo, H. B. Yang, H. W. Liang, S. M. Chen, G. S. Wang, S. H. Yu, A general aerosol-assisted biosynthesis of functional bulk nanocomposites. *Natl. Sci. Rev.* **6**, 64–73 (2019).
27. M. T. I. Mredha, Y. Z. Guo, T. Nonoyama, T. Nakajima, T. Kurokawa, J. P. Gong, A facile method to fabricate anisotropic hydrogels with perfectly aligned hierarchical fibrous structures. *Adv. Mater.* **30**, 201704937 (2018).
28. J. Huang, Y. Zhong, L. Zhang, J. Cai, Extremely strong and transparent chitin films: A high-efficiency, energy-saving, and "green" route using an aqueous KOH/urea solution. *Adv. Funct. Mater.* **27**, 1701100 (2017).
29. U. Ray, S. Zhu, Z. Pang, T. Li, Mechanics design in cellulose-enabled high-performance functional materials. *Adv. Mater.* **33**, 2002504 (2021).
30. F. J. Martin-Martinez, Designing nanocellulose materials from the molecular scale. *Proc. Natl. Acad. Sci. U.S.A.* **115**, 7174–7175 (2018).
31. Y. Maréchal, H. Chanzy, The hydrogen bond network in I_β cellulose as observed by infrared spectrometry. *J. Mol. Struct.* **523**, 183–196 (2000).
32. S. Y. Oh, D. I. Yoo, Y. Shin, H. C. Kim, H. Y. Kim, Y. S. Chung, W. H. Park, J. H. Youk, Crystalline structure analysis of cellulose treated with sodium hydroxide and carbon dioxide by means of x-ray diffraction and FTIR spectroscopy. *Carbohydr. Res.* **340**, 2376–2391 (2005).
33. P. Xia, H. Li, Y. Wang, J. Wang, Processing aramid nanofiber/modified graphene oxide hydrogel into ultrastrong nanocomposite film. *Appl. Surf. Sci.* **545**, 149004 (2021).
34. H. Zhu, S. Zhu, Z. Jia, S. Parvinian, Y. Li, O. Vaaland, L. Hu, T. Li, Anomalous scaling law of strength and toughness of cellulose nanopaper. *Proc. Natl. Acad. Sci. U.S.A.* **112**, 8971–8976 (2015).
35. Y. Hou, Q. F. Guan, J. Xia, Z. C. Ling, Z. He, Z. M. Han, H. B. Yang, P. Gu, Y. Zhu, S. H. Yu, H. Wu, Strengthening and toughening hierarchical nanocellulosevia humidity-mediated interface. *ACS Nano* **15**, 1310–1320 (2021).
36. S. Wang, T. Li, C. Chen, W. Kong, S. Zhu, J. Dai, A. J. Diaz, E. Hitz, S. D. Solares, T. Li, Transparent, anisotropic biofilm with aligned bacterial cellulose nanofibers. *Adv. Funct. Mater.* **28**, 1707491 (2018).
37. X. Zhang, R. Xiong, S. Kang, Y. Yang, V. V. Tsukruk, Alternating stacking of nanocrystals and nanofibers into ultrastrong chiral biocomposite laminates. *ACS Nano* **14**, 14675–14685 (2020).
38. H.-L. Gao, R. Zhao, C. Cui, Y. Zhu, S.-M. Chen, Z. Pan, Y.-F. Meng, S.-M. Wen, C. Liu, H. Wu, S.-H. Yu, Bioinspired hierarchical helical nanocomposite macrofibers based on bacterial cellulose nanofibers. *Natl. Sci. Rev.* **7**, 73–83 (2020).
39. Y. Chen, Q. Zhang, Y. Zhong, P. Wei, X. Yu, J. Huang, J. Cai, Super-strong and super-stiff chitosan filaments with highly ordered hierarchical structure. *Adv. Funct. Mater.* **31**, 2104368 (2021).
40. D. A. Vecchio, S. H. Mahler, M. D. Hammig, N. A. Kotov, Structural analysis of nanoscale network materials using graph theory. *ACS Nano* **15**, 12847–12859 (2021).
41. D. A. Vecchio, M. D. Hammig, X. Xiao, A. Saha, P. Bogdan, N. A. Kotov, Spanning network gels from nanoparticles and graph theoretical analysis of their structure and properties. *Adv. Mater.* **34**, 2201313 (2022).
42. F. Barthelat, Z. Yin, M. J. Buehler, Structure and mechanics of interfaces in biological materials. *Nat. Rev. Mater.* **1**, 16007 (2016).
43. K. Chen, J. Ding, S. Zhang, X. Tang, Y. Yue, L. Guo, A general bioinspired, metals-based synergic cross-linking strategy toward mechanically enhanced materials. *ACS Nano* **11**, 2835–2845 (2017).
44. S. Zhang, W. Shi, T. D. Siegler, X. Gao, F. Ge, B. A. Korgel, Y. He, S. Li, X. Wang, An all-inorganic colloidal nanocrystal flexible polarizer. *Angew. Chem. Int. Ed.* **131**, 8822–8827 (2019).
45. N. L. Nerurkar, B. M. Baker, S. Sen, E. E. Wible, D. M. Elliott, R. L. Mauck, Nanofibrous biologic laminates replicate the form and function of the annulus fibrosus. *Nat. Mater.* **8**, 986–992 (2009).
46. W. Yang, H. Quan, M. A. Meyers, R. O. Ritchie, Arapaima fish scale: One of the toughest flexible biological materials. *Matter* **1**, 1557–1566 (2019).
47. S. Plimpton, Fast parallel algorithms for short-range molecular dynamics. *J. Comput. Phys.* **117**, 1–19 (1995).
48. W. Zhang, A. C. Van Duin, Improvement of the ReaxFF description for functionalized hydrocarbon/water weak interactions in the condensed phase. *J. Phys. Chem. B* **122**, 4083–4092 (2018).
49. W. Humphrey, A. Dalke, K. Schulten, VMD: Visual molecular dynamics. *J. Mol. Graph.* **14**, 33–38 (1996).
50. A. Stukowski, Visualization and analysis of atomistic simulation data with OVITO—The Open Visualization Tool. *Modell. Simul. Mater. Sci. Eng.* **18**, 015012 (2009).
51. E. Braun, Open source code: Calculating an IR spectra from a LAMMPS simulation. Zenodo (2016); https://doi.org/10.5281/zenodo.154672.
52. S. Basu, S. Nag, N. B. Kottan, B. Basu, In silico study on probing atomistic insights into structural stability and tensile properties of Fe-doped hydroxyapatite single crystals. *Sci. Rep.* **12**, 20576 (2022).

Acknowledgments: We thank Y. Ni and K. Wu (Department of Modern Mechanics, USTC) for the useful discussion. This work was supported by the New Cornerstone Science Foundation. It was partially carried out at the USTC Center for Micro and Nanoscale Research and Fabrication. The numerical calculations were carried out on the supercomputing system in the Supercomputing Center of USTC and the Hefei Advanced Computing Center. **Funding:** This work was supported by the National Key Research and Development Program of China (2021YFA0715700 and 2018YFE0202201), the National Natural Science Foundation of China (22293044, 22222508, U1932213, 22005289, 92263102, 12232016, and 12172346), the Major Basic Research Project of Anhui Province (2023z04020009), the Youth Innovation Promotion Association CAS (2022465), the USTC Research Funds of the Double First-Class Initiative (YD9990002019), and the Fundamental Research Funds for the Central Universities (WK2340000112). **Author contributions:** Conceptualization: S.-M.C. and S.-H.Y. Methodology: S.-M.C., G.-Z.W., X.-N.Y., S.-C.Z. Y.Z.H., Y.B.Z., H.-L.G., and H.A.W. Investigation: S.-M.C., G.-Z.W., X.-N.Y., S.-C.Z., Y.Z.H., Z.B.Z., and J.H.L. Visualization: S.-M.C., G.-Z.W., X.-N.Y., and Y.Z.H. Supervision: S.-H.Y., H.-L.G., and Y.B.Z. Writing—original draft: S.-M.C., G.-Z.W., and Y.Z.H. Writing—review and editing: S.-M.C., G.-Z.W., Y.Z.H., H.-L.G., Y.B.Z., and S.-H.Y. **Competing interests:** The authors declare that they have no competing interests. **Data and materials availability:** All data needed to evaluate the conclusions in the paper are present in the paper and/or the Supplementary Materials.

Submitted 4 October 2023
Accepted 5 March 2024
Published 5 April 2024
10.1126/sciadv.adl1884